PCCP

ROYAL SOCIETY OF CHEMISTRY

PAPER

View Article Online
View Journal | View Issue

Cite this: *Phys. Chem. Chem. Phys.*, 2025, **27**, 23313

Planar pentacoordinate germanium stabilized by the 18-valence-electron rule: structural and bonding comparison with silicon analogues

Luz Diego,[a] Diego V. Moreno,[b] David Arias-Olivares[c] and Rafael Islas*[d]

Received 13th August 2025,
Accepted 9th October 2025

DOI: 10.1039/d5cp03108g

rsc.li/pccp

This study examines the $SiE_2M_3^{2+}$ and $GeE_2M_3^{2+}$ clusters (E = P, As, Sb; M = Ca, Sr, Ba) stabilized by 18-valence-electron (18ve). Twelve global minima exhibiting C_{2v} symmetry were identified: six featuring a central silicon atom and six with a central germanium atom. All structures satisfy the geometric criteria for planar pentacoordination as defined by the IUPAC coordination concept. BOMD simulations at 298 and 600 K confirmed their kinetic stability. Using the central atom (Si or Ge) and the $E_2M_3^{2+}$ ring as fragments, the EDA–NOCV analysis reveals that the orbital interaction term (ΔE_{orb}) constitutes the major contribution to stabilization. This is characterized by a dominant s(Si/Ge)–π(ring) coupling, accompanied by π reorganization, with no evidence of an independent Si/Ge–M σ bond. However, IQA analysis reveals that in $SiP_2M_3^{2+}$, all three Si–M interactions are repulsive, resulting in a planar dicoordinate silicon center. In $SiAs_2M_3^{2+}$ and $GeP_2M_3^{2+}$, electrostatic repulsion involving one metal atom (M) prevents the formation of true pentacoordination, resulting instead in planar tetracoordinate centers. Only $GeAs_2M_3^{2+}$ exhibits a genuine planar pentacoordinate germanium center, constituting the first confirmed example of this species stabilized by this specific electron count.

1. Introduction

Systems with planar hypercoordinate atoms are rare and challenge the established principles of chemistry. Research in this field began with planar tetracoordinate carbon atom (ptC), which were initially proposed as a transition state in the interconversion of chiral molecules,[1] and later leading to strategies for its stabilization.[2] In 1991, Schleyer and Boldyrev introduced the first pentaatomic systems featuring a ptC, suggesting that stabilization requires a suitable cavity and strong bond with peripheral atoms.[3] Molecular orbital analysis later revealed that ptC stability arises from three C-ligand σ bonds, a delocalized π-system involving all five atoms, and additional ligand–ligand interactions, consistent with the 18-valence-electron (18ve) rule.[4] Although not a universal rule, given that several ptC structures with different electron counts have been identified,[5–8] the 18ve principle remains an effective theoretical design strategy.[4,9–12] This principle has guided the design of numerous planar tetracoordinate carbon species, including those succsessfully synthesized or detected in the gas phase,[13–18] extending to other main group elements.[12,19–21]

For silicon and germanium atoms, which are isoelectronic analogs of carbon, both theoretical and experimental studies have demonstrated the feasibility of planar tetracoordination. The first experimental evidence was obtained from gas-phase photoelectron spectroscopy of MAl_4^- (M = Si, Ge), reported by Wang *et al.*[22] Subsequently, several ptSi and ptGe species have been synthesized in rigid or macrocyclic ligands.[23–25] From a theoretical standpoint, numerous studies have reported structures featuring a ptSi or ptGe center identified either as global or local minima, stabilized under different criteria. These include systems with halogenated transition-metal ligands XM_4Cl_4 (X = Si, Ge; M = Ni, Pd, Pt);[26] structures with 18ve as $SiIn_4^{2-}$;[27] pentaatomic structures with 14ve in Li_3SiAs^{2-}, $HSiY_3$ (Y = Al, Ga), Ca_3SiAl^-, Mg_4Si^{2-}, C_2LiSi and Si_3Y_2 (Y = Li, Na, K);[28] planar triangular arrangements with D_{3h} symmetry in $X_3Cu_3^+$, $X_3Li_3^+$ (X = Si, Ge) and X_3M_3 (X = C–Pb; M = Li–Cs) formed by three ptX units;[29,30] fan-like structures with C_{2v} symmetry in $C_2Si_2X^q$, XB_2Be_2 and XB_2Bi_2 (X = C, Si, Ge, Sn, Pb; q = +1, 0, −1);[31–33] and, most recently, a ptSi in a rhombic arrangement in $Si_3Cu_3^-$ with 16ve.[34] Despite progress in ptSi and ptGe, planar pentacoordinate silicon (ppSi) and

[a] *Doctorado en Fisicoquímica Molecular, Facultad de Ciencias Exactas, Universidad Andres Bello, Av. República 275, Santiago, 8370146, Chile*
[b] *Laboratorio de Química Computacional, Programa de Química, Universidad de Ciencias Aplicadas y Ambientales (U.D.C.A.), Calle 222 #55-37, Bogotá 111166, Colombia*
[c] *Center of Applied Nanoscience (CANS), Facultad de Ciencias Exactas, Universidad Andres Bello, Av. República 275, Santiago 8370146, Chile*
[d] *Departamento de Ciencias Químicas, Facultad de Ciencias Exactas, Universidad Andres Bello, Av. República 275, Santiago, 8370146, Chile. E-mail: rafael.islas@unab.cl*

germanium (ppGe) remain far less explored. Achieving planar pentacoordination is more challenging because the interactions between the central Si or Ge and neighboring metals are often weak or even repulsive, making it difficult to stabilize the system.

In 2020, the first ppSi and ppGe species were identified within the XMg_4Y^- (X = Si, Ge; Y = In, Tl) and $SiMg_3In_2$ systems.[35] These designs were based on the "electronic localization" approach, which consists of replacing one or two peripheral atoms in XMg_5^{2-} with more electronegative elements, to reduce electronic repulsion and strengthen X–Y bonding, thereby stabilizing the planar pentacoordinate center. In addition, several planar hypercoordinate configurations of silicon based on SiO_3 units surrounded by alkali metals in SiO_3M^-, SiO_3M_2 and $SiO_3M_3^+$ (M = Li, Na) have been described, where EDA–NOCV bonding analysis reveals that the high stability and planarity in these systems is due to dative interactions ($M \leftarrow SiO_3$) mediated by the metal s, p and d vacant orbitals, and Si–O multiple bonds.[36]

Building on this context, the 18ve rule is used here as a design guideline for achieving planar pentacoordination. This rule has been widely applied to predict numerous planar pentacoordinate carbon (ppC) species.[37–44] For instance, the $CO_2Li_3^+$ cation has been reported to exhibit a global minimum with a ppC, when evaluated under the IUPAC coordination-number concept, along with interatomic distances and Wiberg bond indices.[45] However, a subsequent IQA analysis showed electrostatic repulsion between C and Li, indicating a planar dicoordinate carbon.[46] The same study extended the scope to $CE_2M_3^+$ systems (E = S–Te; M = Li–Cs), identifying five global minima with a ppC, all consistent with 18ve. Following this principle, we extend the design by replacing carbon with Si and Ge, substituting chalcogens with pnictogens (E = P, As, Sb), and employing alkaline-earth metals (M = Be–Ba, Fig. 1). Systems containing Be or Mg exhibited imaginary vibrational modes and therefore did not correspond to real minima, while Ca, Sr, and Ba presented stable minima (see Tables S1 and S2). Unlike previous designs based on Mg and alkali metals, the heavier alkaline earth metals (Ca, Sr, Ba) offer a more favorable platform for 18ve-guided design with silicon or germanium centers. While all global minima satisfy the geometric criterion (IUPAC), only $GeAs_2M_3^{2+}$ fulfills the energetic IQA criterion for genuine pentacoordination.

2. Computational details

This study focuses on a total of 30 pentaatomic combinations: fifteen with the formula $SiE_2M_3^{2+}$ and fifteen with $GeE_2M_3^{2+}$ (E = P, As, Sb; M = Be–Ba). All systems were designed to satisfy the 18ve rule. The initial structures were built with C_{2v} symmetry, placing the Si or Ge atom at the center. Geometry optimizations at the PBE0[47]-D3[48]/def2-TZVP level[49] revealed eighteen planar minima; the remaining combinations were discarded because harmonic frequency analysis revealed one or more imaginary vibrational modes (see Tables S1 and S2). These eighteen minima served as starting points for a more extensive potential energy surface (PES) exploration using a modified genetic algorithm implemented in the GLOMOS[50,51] program at the PBE0/SDDAll[52,53] level of theory. The search used an initial population of 80 candidate structures, applied 30 crossover operations and 30 mutation operations in each generation, and proceeded for up to 10 generations. Isomers within 30 kcal mol^{-1} were reoptimized at the PBE0-D3 level using aug-cc-pVTZ and aug-cc-pVTZ-PP (for Sb, Sr, and Ba);[54–56] harmonic frequency analysis confirmed them as true minima. Single-point energies were refined at the CCSD(T)[57]/aug-cc-pVTZ level, including zero-point energy corrections computed at the PBE0-D3/aug-cc-pVTZ level. Wavefunction stability checks and T_1 diagnostics indicated negligible multireference character.[58] Finally, all singlet minima were recalculated as triplets to assess spin-state preferences.

The dynamical behavior of the system was explored through Born–Oppenheimer molecular dynamics (BOMD)[59] simulations at 298 K and 600 K, carried out at the PBE0-D3/SDDAll level for 20 ps with a 1 fs time step. Since this program implements only a velocity-rescaling thermostat *via* the ADMP method,[60] the simulations were run using the FULLSCF option to ensure equivalence with standard BOMD. All calculations were performed using the Gaussian 16.[61]

The electron distribution was evaluated using Wiberg bond indices (WBI)[62] and natural population analysis (NPA),[63] both implemented in NBO 7.0.[64] For a more detailed analysis of the nature of the bonds, the adaptive natural density partitioning (AdNDP)[65] method, implemented in Multiwfn, was used.[66] These calculations were performed at the PBE0-D3/aug-cc-pVTZ level, and the graphical representations were generated using VMD 1.9.3.[67,68]

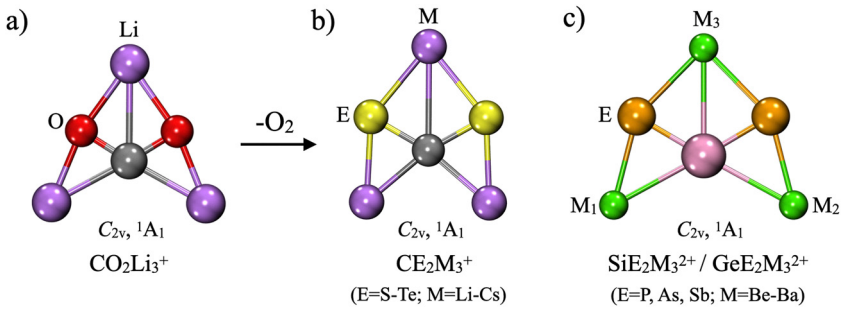

Fig. 1 Graphical representation of the global minimum ppC in (a) the $CO_2Li_3^+$ cation and in (b) the $CE_2M_3^+$ (E = S–Te; M = Li–Cs) type systems. (c) The new $SiE_2M_3^{2+}$ and $GeE_2M_3^{2+}$ (E = P, As, Sb; M = Be–Ba) system proposed in this work.

Interatomic interaction energies (V_{int}) were decomposed using the interaction quantum atoms (IQA) method.[69] This approach partitions V_{int} between atomic basins into a Coulomb term V_C (encompassing all classical electrostatic components) and an exchange–correlation term V_{XC} (capturing purely quantum contributions, including Pauli repulsion and electron correlation), which are commonly associated with ionic and covalent bonding, respectively. By convention, $V_{int} < 0$ denotes attraction and $V_{int} > 0$ denotes repulsion. All IQA calculations were performed in AIMAll[70] using wavefunctions generated at the PBE0-D3/aug-cc-pVTZ level.

Energy decomposition analysis (EDA) combined with ETS–NOCV was performed within the framework of relativistic density functional theory using the Amsterdam Density Functional (ADF 2024-103) code.[71] The zeroth-order regular approximation (ZORA)[72] was applied to account for scalar relativistic effects. Calculations were carried out using the PBE0-D3/TZVP[73] level. All systems were fragmented following the same scheme: one fragment corresponds to the central atom, and the second fragment corresponds to the surrounding "ring". The interaction energy was decomposed according to the Morokuma–Ziegler scheme into the following components:

$$\Delta E_{int} = \Delta E_{Pauli} + \Delta E_{orb} + \Delta E_{elstat} + \Delta E_{disp}$$

where int, Pauli, orb, elstat, and disp denote the total interaction energy, Pauli repulsion, orbital interaction (orbital mixing), electrostatic interaction, and dispersion correction, respectively.[74,75] Extended transition state (ETS) analysis was combined with EDA to examine the decomposition of ΔE_{orb}, and the characteristics of the orbital mixing terms. Each fragment is associated with a set of natural orbitals for chemical valence (NOCV),[76] and its deformation density, $\Delta\rho$, is represented by a sum of complimentary eigenfunctions (Ψ_{-k}, Ψ_{+k}) weighted by their corresponding eigenvalues:

$$\Delta\rho = \sum \lambda_k \left(-\psi_{-k}{}^2 + \psi_{+k}{}^2\right)$$

where k runs over all NOCV pairs. The deformation density plots provide insight into electron flow and the symmetry involved. In this work, charge flows from red regions ($\Delta_{rho} > 0$), to blue regions ($\Delta_{rho} < 0$).

3. Result and discussion

3.1. Structure and energy

Out of the thirty configurations examined, eighteen were confirmed as true minima, each featuring a central Si or Ge atom in a planar pentacoordinate environment. Exploration of the potential energy surface identified twelve global minima, distributed between six Si-centered structures in $SiE_2M_3^{2+}$ and six Ge-centered structures in $GeE_2M_3^{2+}$ (E = P, As; M = Ca, Sr, Ba). Fig. 2 shows some of the low-energy isomers, while the remaining isomers of each system are depicted in Fig. S1–S12. For systems with E = As, the second most stable isomer is between 2.1 and 5.1 kcal mol^{-1} above the global minimum in $SiAs_2M_3^{2+}$, and between 0.1 and 2.2 kcal mol^{-1} in $GeAs_2M_3^{2+}$ (M = Ca, Sr,

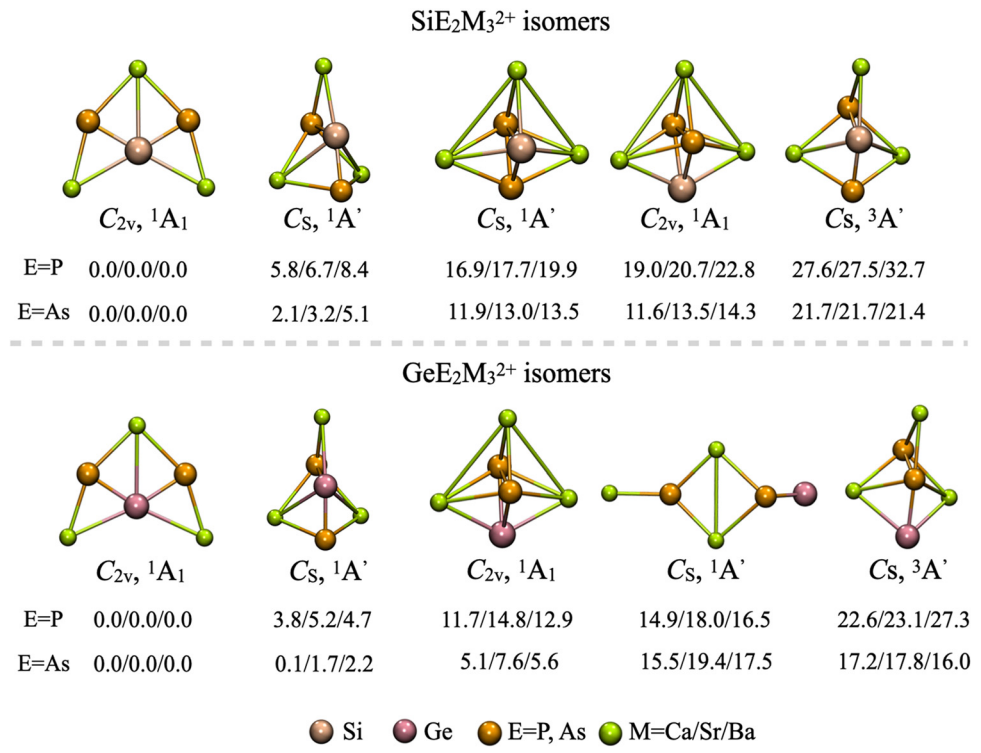

Fig. 2 Structures and relative energies in kcal mol^{-1} of the low-energy isomers in $SiE_2M_3^{2+}$ and $GeE_2M_3^{2+}$ (E = P, As; M = Ca, Sr, Ba) computed at the CCSD(T)/aug-cc-pVTZ//PBE0-D3/aug-cc-pVTZ level of theory including ZPE corrections from PBE0-D3/aug-cc-pVTZ. Point group symmetries and spectroscopic states are indicated.

Ba). To ensure structural accuracy and confirm that these are true minima, additional optimizations and frequency analysis were performed at the MP2[77]/aug-cc-pVTZ level but only for the global minimum and the lowest energy local isomer, due to the small energy difference between them. The geometries obtained at the MP2 level are consistent with those optimized with PBE0-D3, with no significant differences in bond lengths or overall geometry.

Single-point energy calculations were performed on these structures at the CCSD(T)/aug-cc-pVTZ//MP2/aug-cc-pVTZ level of theory, and their values are shown in Fig. S13. Although the energy corrections obtained with CCSD(T)//MP2 are slightly larger than those calculated with CCSD(T)//PBE0-D3, both theoretical levels agree that the global minimum corresponds to a structure with a Si or Ge center in a planar pentacoordinate environment. The diagnostic T_1 values for all global minima are below the 0.02 threshold, validating the use of a single-reference formalism and lending confidence to the accuracy of the computed energies at the CCSD(T) level. The triplet isomers ($^3A'$ state, C_s symmetry), shown in the last column of Fig. 2, lie between 16 and 33 kcal mol^{-1} above the singlet global minimum. Although some triplets present T_1 values below 0.034, their high energy rules out that they compete in the relative stability of the system. Regarding the remaining six minima with Si and Ge centers in $SiSb_2M_3^{2+}$ and $GeSb_2M_3^{2+}$ (M = Ca, Sr, Ba), these correspond to local minima with energies 1.5 and 4 kcal mol^{-1} above the global minimum, respectively (see Fig. S14–S19).

To evaluate the kinetic stability of the proposed systems, four representative global minima were selected in total, two with a Si center and two with a Ge center, from the $SiE_2Ca_3^{2+}$ and $GeE_2Ca_3^{2+}$ families with E being P and As. BOMD simulations were then performed at 298 and 600 K. Videos included in the SI show that the structures tend to maintain their planarity, with flexible motions of the Ca atoms around the SiE_2 and GeE_2 fragment. At 600 K, more pronounced thermal fluctuations are observed, particularly in the Ca atoms, which occasionally deviate from the plane without inducing structural rearrangements or isomerization processes. These results support kinetic persistence at both room and moderately elevated temperatures.

All global minima of $SiE_2M_3^{2+}$ and $GeE_2M_3^{2+}$ (E = P, As; M = Ca, Sr, Ba) show that the Si/Ge–E distances remain remain constant as M increases and increase from P to As. Hereafter, the notation Si/Ge means ''silicon or germanium''. The distances listed in Table 1 are shorter than the sums of the corresponding Pyykkö single-bond covalent radii (2.27 and 2.37 Å for Si–P and Si–As; 2.32 and 2.42 Å for Ge–P and Ge–As). Conversely, the Si/Ge–$M_{1,2}$ and Si/Ge–M_3 distances increase with the size of E and M. When compared to the Pyykkö covalent radii (2.87, 3.01 and 3.12 Å for Si–Ca, Si–Sr and Si–Ba; 2.92, 3.06 and 3.17 for Ge–Ca, Ge–Sr and Ge–Ba, respectively),[78] it is observed that the Si/Ge–$M_{1,2}$ distances are slightly larger, while for Si/Ge–M_3 they are longer but shorter than the sum of the van der Waals radii.[79]

Natural population analysis (NPA) reveals negative charges on the center Si/Ge and on E, balanced by positive charges on $M_{1,2}$ and M_3 (see Table 1). Generally, variations in the electronegativity of both E and the central atom influence the charge distribution: progressing from phosphorus (P) to arsenic (As) shifts electron density toward the central atom, whereas moving from Si to Ge directs charge density toward E. Notably, the charges on the metal sites (M) remain largely invariant across these changes.

The low WBI values for Si/Ge–$M_{1,2}$ (0.07–0.09) and Si/Ge–M_3 (0.003–0.005) indicated an insignificant covalent contribution (minimal overlap) with interactions dominated by electrostatic, whereas the high values for the Si/Ge–E (1.43–1.49) are consistent with strong two-center covalent bond. In line with the ppC systems reported by Leyva–Parra and co-workers, where C–E bonding is covalent and C–M interactions are weak and largely electrostatic, our Si/Ge-centered systems retain this pattern but the charge distribution changes: as C → Si → Ge, the center becomes less negative, E more negative, and M more positive. In addition, the Si/Ge–E bonds lengthen from P to As, and the Si/Ge–M interaction grows from Ca to Sr to Ba, while remaining weak and predominantly electrostatic.

According to the IUPAC coordination concept,[80] the observed arrangement, supported by interatomic distances,

Table 1 HOMO–LUMO gap (gap, in eV), bond distances (r, Å), natural population analysis (NPA) charges (q, in |e|) and the Wiberg bond indices (WBIs) for the global minima in $SiE_2M_3^{2+}$ and $GeE_2M_3^{2+}$ (E = P, As and M = Ca, Sr, Ba) evaluated at the PBE0-D3/aug-cc-TZVP level

	PG	Gap	$r_{Si-M_{1,2}}$	r_{Si-M_3}	r_{Si-E}	q(Si)	q($M_{1,2}$)	q(M_3)	q(E)	$WBI_{Si-M_{1,2}}$	WBI_{Si-M_3}	WBI_{Si-E}
$SiP_2Ca_3^{2+}$	C_{2v}	3.46	2.87	3.01	2.18	−0.53	+1.70	+1.71	−1.30	0.093	0.003	1.48
$SiP_2Sr_3^{2+}$	C_{2v}	3.23	3.03	3.19	2.18	−0.52	+1.74	+1.75	−1.35	0.069	0.003	1.49
$SiP_2Ba_3^{2+}$	C_{2v}	3.31	3.20	3.38	2.18	−0.49	+1.74	+1.77	−1.38	0.071	0.003	1.48
$SiAs_2Ca_3^{2+}$	C_{2v}	3.16	2.87	3.06	2.29	−0.73	+1.69	+1.70	−1.17	0.070	0.004	1.48
$SiAs_2Sr_3^{2+}$	C_{2v}	2.95	3.04	3.26	2.29	−0.72	+1.73	+1.74	−1.24	0.070	0.004	1.49
$SiAs_2Ba_3^{2+}$	C_{2v}	3.14	3.21	3.45	2.29	−0.68	+1.73	+1.75	−1.26	0.072	0.005	1.49
	PG	Gap	$r_{Ge-M_{1,2}}$	r_{Ge-M_3}	r_{Ge-E}	q(Ge)	q($M_{1,2}$)	q(M_3)	q(E)	$WBI_{Ge-M_{1,2}}$	WBI_{Ge-M_3}	WBI_{Ge-E}
$GeP_2Ca_3^{2+}$	C_{2v}	3.38	2.93	3.10	2.26	−0.50	+1.71	+1.71	−1.32	0.093	0.003	1.43
$GeP_2Sr_3^{2+}$	C_{2v}	3.21	3.08	3.27	2.26	−0.50	+1.75	+1.75	−1.37	0.069	0.003	1.45
$GeP_2Ba_3^{2+}$	C_{2v}	3.31	3.24	3.45	2.26	−0.46	+1.75	+1.77	−1.43	0.071	0.003	1.44
$GeAs_2Ca_3^{2+}$	C_{2v}	3.17	2.93	3.15	2.37	−0.69	+1.70	+1.70	−1.20	0.070	0.004	1.44
$GeAs_2Sr_3^{2+}$	C_{2v}	2.95	3.08	3.32	2.37	−0.69	+1.74	+1.74	−1.26	0.070	0.004	1.46
$GeAs_2Ba_3^{2+}$	C_{2v}	3.05	3.26	3.52	2.37	−0.65	+1.73	+1.75	−1.29	0.072	0.005	1.45

NPA charges and WBI, fulfills the geometric criteria for planar pentacoordination at the central atoms. The nature and energetic contribution of the individual interactions are examined in detail in subsequent sections.

3.2. Chemical bond

AdNDP analysis, as an extension of the NBO approach, allows the recovery of lone pairs (LPs), classical 2c–2e bonds and multicenter delocalized bonds of the nc–2e type ($n \geq 3$). In the global minima, one LP is recovered on each E (ON = 1.93–1.95 |e|) and one LP on Si/Ge oriented toward the metal-ring cavity (ON = 1.83–1.89 |e|). Two localized Si/Ge–E 2c–2e σ bonds with high occupancies (ON = 1.96–1.97 |e|) are also identified, together with a 3c–2e σ bond along the $M_{1,2}$–E–M_3 edge with a major contribution from E. In addition, two delocalized 3c–2e π bonds are recovered within the E–Si/Ge–E fragment: the first is concentrated mainly on the E atoms, exhibiting extended lone-pair character, while the second spans the entire E–Si/Ge–E fragment. The graphical representation is shown in Fig. 3a, and the corresponding occupation numbers (ON) are reported in Table S3. Both π distributions correspond to the canonical molecular orbitals (CMOs) HOMO and HOMO–3, respectively; their shapes are shown in Fig. 3b and their CMOs energies are listed in Table S4. No localized 2c–2e Si/Ge–M σ bond is recovered.

To probe the nature and strength of the interactions, energy decomposition analysis combined with natural orbitals for chemical valence (EDA–NOCV) was employed, using the Si/Ge center and the $E_2M_3^{2+}$ ring as fragments. The total interaction energy (ΔE_{int}) ranges from −213.3 to −242.6 kcal mol^{-1} and is more stabilizing for Si than for Ge and for P than for As. The orbital term (ΔE_{orb}) dominates the stabilization and contributes between 64 and 70% of the attractive interaction. The electrostatic term (ΔE_{elstat}) accounts for between 30 and 36%, whereas dispersion (ΔE_{disp}) is minor. Pauli repulsion (ΔE_{Pauli}) tends to decrease along the series Si → Ge, P → As and Ca → Sr → Ba, consistent with more diffuse electron clouds in heavier atoms leading to reduced steric repulsion. Overall, lighter centers (Si) and pnictogens (P) enhance the orbital (covalent) component, while Si → Ge or P → As substitutions modestly increase electrostatic character; the effect of M (Ca → Sr → Ba) is minor (see Table 2).

Table 2 EDA result of the Si (S, $3s^23p^2$) or Ge (S, $4s^24p^2$) + $E_2M_3^{2+}$ (S) as interacting fragments at the PBE0-D3/TZ2P-ZORA//PBE0-D3/aug-cc-pVTZ level. All energy values are in kcal mol^{-1}

System	ΔE_{orb}	ΔE_{elstat}	ΔE_{disp}	ΔE_{Pauli}	ΔE_{int}	$\%\Delta E_{orb}$	$\%\Delta E_{elstat}$
$SiP_2Ca_3^{2+}$	−812.6	−358.1	0.2	929.2	−241.3	69	31
$SiP_2Sr_3^{2+}$	−806.6	−353.4	0.2	917.2	−242.6	70	30
$SiP_2Ba_3^{2+}$	−786.9	−348.8	0.6	895.1	−240.1	69	31
$SiAs_2Ca_3^{2+}$	−754.4	−361.4	0.0	884.5	−231.3	68	32
$SiAs_2Sr_3^{2+}$	−744.2	−353.8	0.0	866.3	−231.8	68	32
$SiAs_2Ba_3^{2+}$	−725.8	−347.8	0.3	844.0	−229.3	68	32
$GeP_2Ca_3^{2+}$	−712.8	−363.4	0.2	855.6	−220.6	66	34
$GeP_2Sr_3^{2+}$	−712.3	−362.7	0.3	852.6	−222.1	66	34
$GeP_2Ba_3^{2+}$	−699.5	−359.9	0.7	837.9	−220.7	66	34
$GeAs_2Ca_3^{2+}$	−671.6	−369.8	0.0	828.2	−213.3	64	36
$GeAs_2Sr_3^{2+}$	−666.7	−365.4	0.1	817.9	−214.1	65	35
$GeAs_2Ba_3^{2+}$	−653.7	−360.6	0.5	801.3	−212.5	64	36

Decomposition of ΔE_{orb} into NOCV pairs (Fig. 4, shown for the representative $SiP_2Ca_3^{2+}$) yields four homologous contributions across the series. The first NOCV (∼40% of ΔE_{orb}) represents a σ-bond between the s-orbital of the central atom and a π-orbital from the ring (mainly E atoms). The second (∼20%) corresponds to a π-orbital reorganization in both fragments, and the third (∼20%) to π-cloud formation *via* intrafragment reorganization. Together they recover ∼80% of ΔE_{orb}. The fourth NOCV represents a center-ring

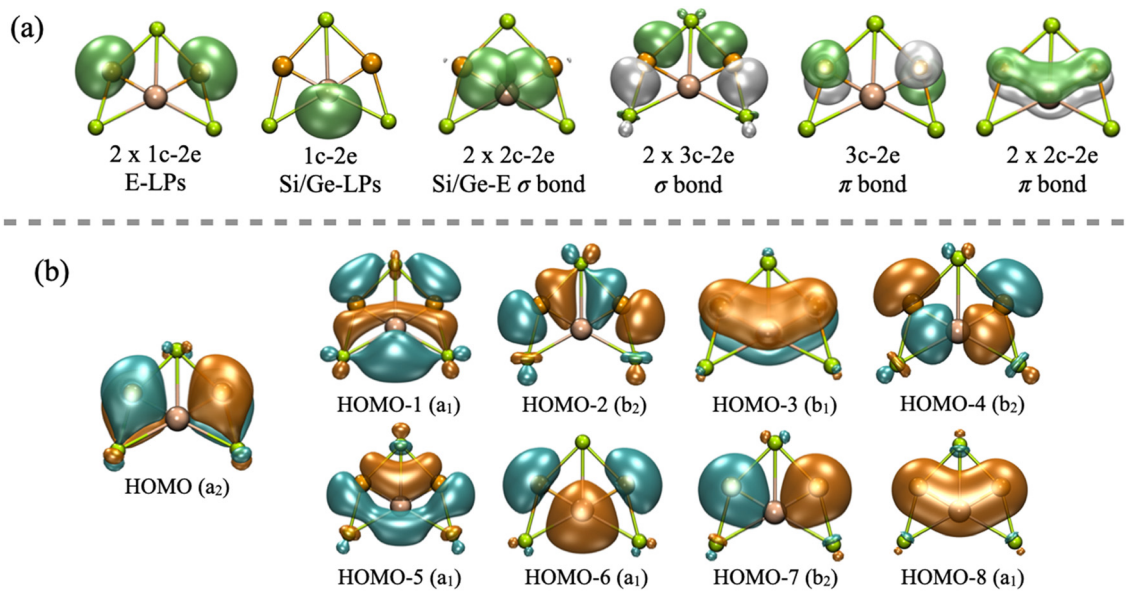

Fig. 3 Graphical representation of (a) bonding pattern from AdNDP analysis, calculated for the global minima ppSi and ppGe in $SiE_2M_3^{2+}$ and $GeE_2M_3^{2+}$ (E = P, As; M = Ca, Sr, Ba) at the PBE0-D3/aug-cc-pVTZ level and (b) canonical molecular orbitals (CMOs).

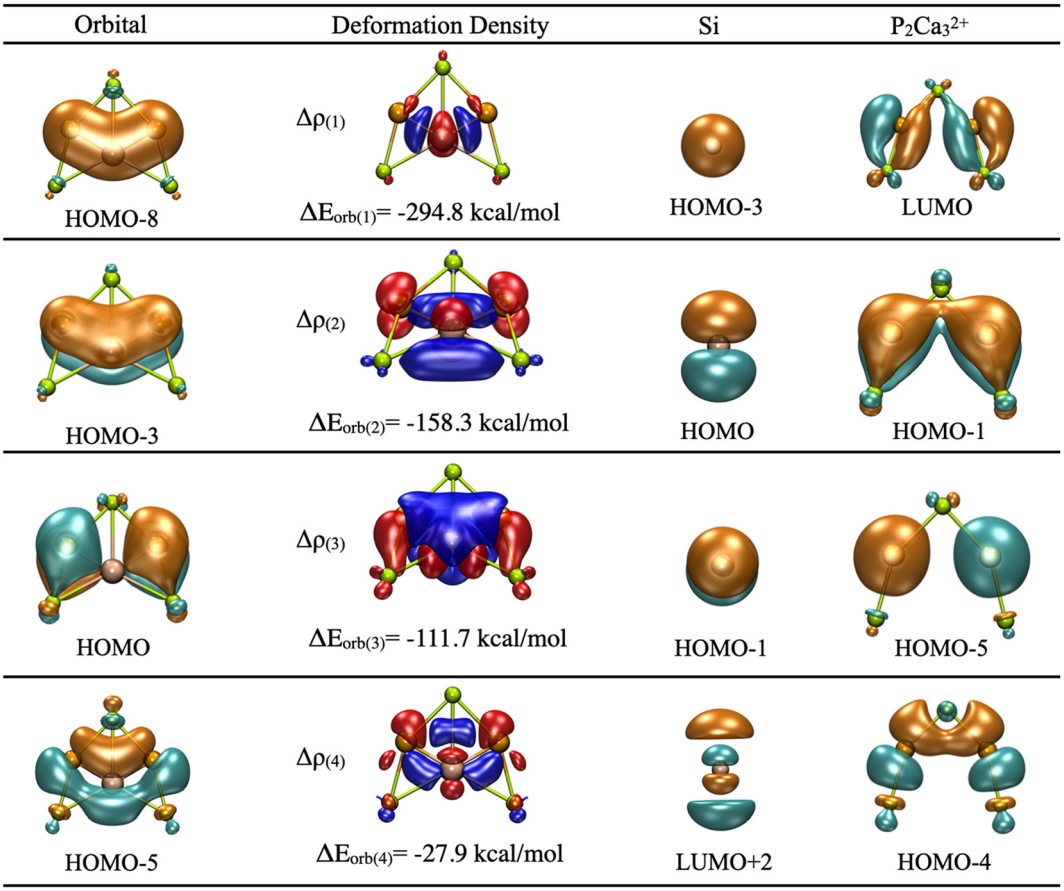

Fig. 4 Plot of the deformation densities, $\Delta\rho_{(1)-(4)}$ corresponding to $\Delta E_{orb(1)-(4)}$ and the related interacting orbitals of the fragments in the $SiP_2Ca_3^{2+}$ system at the PBE0-D3/TZ2P-ZORA level. The charge flow of the deformation densities is from red to blue. The isovalue for $\Delta\rho_{(1)}$ and $\Delta\rho_{(2)}$ is 0.001 a.u. and for the rest is 0.0005 a.u.

electron-density reorganization rather than an independent two-center Si/Ge–M σ bond, thus enhancing overall cohesion. Polarization increases from Si to Ge but does not develop into a distinct two-center σ bond.

Table 3 Energy components of IQA (in kcal mol^{-1}) between atom pairs in of $TtE_2M_3^{2+}$ (Tt = Si, Ge; E = P, As; M = Ca, Sr, Ba) at PBE0-D3/aug-cc-pVTZ level. ΔE_{IQA} represents the integration error. The reported values include the total interatomic interaction energy, the Coulomb component, and the exchange–correlation component

	$SiP_2Ca_3^{2+}$	$SiP_2Sr_3^{2+}$	$SiP_2Ba_3^{2+}$	$SiAs_2Ca_3^{2+}$	$SiAs_2Sr_3^{2+}$	$SiAs_2Ba_3^{2+}$	$GeP_2Ca_3^{2+}$	$GeP_2Sr_3^{2+}$	$GeP_2Ba_3^{2+}$	$GeAs_2Ca_3^{2+}$	$GeAs_2Sr_3^{2+}$	$GeAs_2Ba_3^{2+}$
ΔE_{IQA}	0.0	0.0	0.0	0.0	0.0	0.0	0.0	0.0	0.0	0.0	0.0	0.0
V_{IQA}^{Int} (Tt − E)	−436.1	−439.1	−439.4	−224.6	−230.3	−243.0	−173.7	−173.7	−180.0	−130.7	−131.6	−139.6
V_{C}^{Int} (Tt − E)	−282.2	−285.5	−289.2	−59.9	−66.5	−83.6	−4.7	−4.2	−13.6	31.8	30.9	19.8
V_{XC}^{Int} (Tt − E)	−153.9	−153.6	−150.2	−164.7	−163.8	−159.4	−169.0	−169.5	−166.4	−162.5	−162.5	−159.4
V_{IQA}^{Int} (Tt–$M_{1,2}$)	63.2	60.5	64.7	−41.9	−37.2	−19.0	−58.8	−60.2	−45.4	−99.2	−96.2	−76.7
V_{C}^{Int} (Tt–$M_{1,2}$)	86.4	83.8	89.5	−15.4	−11.2	8.2	−36.2	−37.3	−20.9	−74.3	−71.5	−50.5
V_{XC}^{Int} (Tt–$M_{1,2}$)	−23.2	−23.3	−24.8	−26.5	−26.0	−27.3	−22.6	−22.9	−24.5	−25.0	−24.7	−26.2
V_{IQA}^{Int} (Tt–M_3)	162.5	157.1	149.5	45.3	47.8	54.8	8.9	7.8	13.7	−33.8	−31.0	−20.1
V_{C}^{Int} (Tt–$M_{1,2}$)	168.6	162.6	155.6	53.8	55.3	62.8	17.0	15.4	22.1	−24.6	−22.6	−11.0
V_{XC}^{Int} (Tt–$M_{1,2}$)	−6.1	−5.5	−6.1	−8.5	−7.5	−7.9	−8.1	−7.6	−8.4	−9.2	−8.4	−9.1
V_{IQA}^{Int} (E–$M_{1,2}$)	−379.6	−373.9	−344.2	−301.3	−299.8	−278.6	−302.4	−298.7	−275.9	−262.8	−261.1	−241.6
V_{C}^{Int} ($E - M_{1,2}$)	−315.9	−313.0	−274.5	−242.2	−242.7	−213.3	−238.7	−238.2	−206.9	−202.9	−203.6	−176.1
V_{XC}^{Int} (E–$M_{1,2}$)	−63.7	−60.9	−69.7	−59.1	−57.1	−65.3	−63.7	−60.5	−69.1	−59.9	−57.5	−65.5
V_{IQA}^{Int} (E–M_3)	−346.4	−314.4	−312.2	−275.0	−273.6	−251.8	−270.2	−267.5	−244.8	−235.6	−234.6	−214.3
V_{C}^{Int} (E–$M_{1,2}$)	−301.6	−297.5	−263.3	−232.4	−231.6	−205.2	−225.9	−224.0	−196.5	−193.0	−192.6	−167.8
V_{XC}^{Int} (E–$M_{1,2}$)	−44.8	−43.9	−48.9	−42.6	−42.0	−46.6	−44.3	−43.5	−48.3	−42.5	−42.0	−46.5

These findings again raise the question of what interaction links the Si/Ge center to M. To complement EDA–NOCV and apply an energy-based interatomic criterion, we next employ the Interacting Quantum the Atoms (IQA) framework. Table 3 summarizes the interatomic components for representative Tt–E, Tt–$M_{1,2}$, and Tt–M_3 pairs (Tt = Si or Ge). Across all global minima, Tt–E interactions are attractive and typically display a comparatively large V_{XC}, except for the $SiP_2M_3^{2+}$ series, where Si–P is predominantly V_C. Planar pentacoordination arises only when all five interactions (two Tt–E and three Tt–M) are attractive in IQA, a condition met only by $GeAs_2M_3^{2+}$, whose Ge–M interactions are largely Coulombic. By contrast, Tt–M behavior depends on both the pnictogen and the metal: in $SiP_2M_3^{2+}$, Si–$M_{1,2}$ and Si–M_3 are repulsive (dicoordination); in $SiAs_2M_3^{2+}$, Si–$M_{1,2}$ becomes attractive with $V_{XC} > V_C$ while Si–M_3 remains repulsive (tetracoordination); in $GeP_2M_3^{2+}$, Ge–$M_{1,2}$ is attractive with $V_C > V_{XC}$ for light metals and shifts toward larger V_{XC} as M becomes heavier, whereas Ge–M_3 remains repulsive (tetracoordination); in $GeAs_2M_3^{2+}$, all three Ge–M interactions are attractive and predominantly Coulombic. Thus, IQA analysis shows that the specific Ge–M interactions enabling genuine pentacoordination are chiefly electrostatic, which reconciles the strong global orbital stabilization found by EDA–NOCV with the absence of a localized Tt–M two-center σ bond.

Even when true planar pentacoordination at the center is not achieved, the structure remains bound because the E–$M_{1,2}$ and E–M_3 interatomic interactions, attractive and predominantly Coulombic, compensate for the lack of bonding between the center and some metals, thereby sustaining the planar geometry.

4. Conclusions

Guided by the 18-valence-electron (18ve) design principle, twelve C_{2v}-symmetric global minima were identified for the $SiE_2M_3^{2+}$ and $GeE_2M_3^{2+}$ systems (E = P, As; M = Ca, Sr, Ba). Their stability was assessed through potential energy surface (PES) exploration and Born–Oppenheimer molecular dynamics (BOMD) simulations at 298 and 600 K. According to the IUPAC coordination concept, all identified minima satisfy the geometric criteria for planar pentacoordination at the silicon and germanium centers. Energy decomposition analysis combined with natural orbitals for chemical valence (EDA–NOCV) indicates that orbital interactions (ΔE_{orb}) contribute predominantly to the stabilization, primarily *via* σ coupling between the central *s* orbital of Si/Ge and the π system of the $E_2M_3^{2+}$ ring. The three principal NOCV pairs account for approximately 80% of ΔE_{orb}, dominated by this σ *s*(Si/Ge)–π(ring) interaction, along with two π orbital reorganizations. A fourth NOCV pair corresponds to center-ring polarization and does not represent an independent two-center Si/Ge–M σ bond. Using the interacting quantum atoms (IQA) approach as an energy-based interatomic criterion, distinctions are made between systems that are only geometrically pentacoordinate and those that are energetically tetra- or dicoordinate. In $SiP_2M_3^{2+}$ species, all three Si–M interactions are repulsive, consistent with planar dicoordination. In $SiAs_2M_3^{2+}$ and $GeP_2M_3^{2+}$, the interaction of the center with one of the metals is not attractive, suggesting of planar tetracoordination. Only $GeAs_2M_3^{2+}$ exhibits genuine planar pentacoordination, with attractive and predominantly Coulombic Ge–M interactions, while Ge–E interactions are attractive with a significant exchange–correlation covalent contribution. This analysis suggests that peripheral E–M interactions contribute to maintaining the planar geometry even in the absence of a localized Si/Ge–M bond and that the global minimum of $GeAs_2M_3^{2+}$ exhibits a ppGe, consistent with the 18ve rule.

Conflicts of interest

There are no conflicts to declare.

Data availability

All data supporting this article are provided in the supplementary information (SI). The supplementary information (SI) contains relevant data supporting this study, including Cartesian coordinates of the investigated clusters, comprehensive AdNDP representations, and molecular dynamics simulation videos. See DOI: **https://doi.org/10.1039/d5cp03108g**.

Acknowledgements

We extend our heartfelt gratitude to Dr. Mario Duque, Administrator of the UNAB Computing Center, for his invaluable support. His unwavering commitment and expertise have greatly contributed to the success of our work, and we are sincerely appreciative of his assistance throughout this process. L. D. acknowledges support from the Agencia Nacional de Investigación y Desarrollo (ANID, Chile), Programa de Becas, Beca de Doctorado Nacional 2023-21231670.

References

1 H. J. Monkhorst, *Chem. Commun.*, 1968, 1111–1112.
2 R. Hoffmann, R. W. Alder and C. F. Wilcox Jr, *J. Am. Chem. Soc.*, 1970, **92**, 4992–4993.
3 P. V. R. Schleyer and A. I. Boldyrev, *J. Chem. Soc., Chem. Commun.*, 1991, (21), 1536–1538.
4 A. I. Boldyrev and J. Simons, *J. Am. Chem. Soc.*, 1998, **120**, 7967–7972.
5 Z. H. Cui, M. Contreras, Y. H. Ding and G. Merino, *J. Am. Chem. Soc.*, 2011, **133**, 13228–13231.
6 J. Guo, H. Chai, Q. Duan, J. Qin, X. Shen, D. Jiang, J. Hou, B. Yan, Z. Li and F. Gu, *Phys. Chem. Chem. Phys.*, 2016, **18**, 4589–4593.
7 S. Vogt-Geisse, J. I. C. Wu, P. V. R. Schleyer and H. F. Schaefer III, *J. Mol. Model.*, 2015, **21**, 217.

8 H. F. Zheng, S. Yu, T. D. Hu, J. Xu and Y. H. Ding, *Phys. Chem. Chem. Phys.*, 2018, **20**, 26266–26272.
9 C. Crigger, B. K. Wittmaack, M. Tawfik, G. Merino and K. J. Donald, *Phys. Chem. Chem. Phys.*, 2012, **14**, 14775–14783.
10 A. C. Castro, M. Audiffred, J. M. Mercero, J. M. Ugalde, M. A. Méndez-Rojas and G. Merino, *Chem. Phys. Lett.*, 2012, **519-520**, 29–33.
11 Z. H. Cui, Y. H. Ding, J. L. Cabellos, E. Osorio, R. Islas, A. Restrepo and G. Merino, *Phys. Chem. Chem. Phys.*, 2015, **17**, 8769–8775.
12 X. D. Jia and Z. W. Du, *Phys. Chem. Chem. Phys.*, 2023, **25**, 4211–4215.
13 G. Erker, M. Albrecht, C. Krueger and S. Werner, *Organometallics*, 1991, **10**, 3791–3793.
14 X. Li, L. S. Wang, A. I. Boldyrev and J. Simons, *J. Am. Chem. Soc.*, 1999, **121**, 6033–6038.
15 X. Li, H. F. Zhang, L. S. Wang, G. D. Geske and A. I. Boldyrev, *Angew. Chem.*, 2000, **112**, 3776–3778.
16 C. J. Zhang, P. Wang, X. L. Xu, H. G. Xu and W. J. Zheng, *Phys. Chem. Chem. Phys.*, 2021, **23**, 1967–1975.
17 W. Siebert and A. Gunale, *Chem. Soc. Rev.*, 1999, **28**, 367–371.
18 G. Merino, M. A. Méndez Rojas, A. Vela and T. Heine, *J. Comput. Chem.*, 2007, **28**, 362–372.
19 G. Castillo-Toraya, M. Orozco-Ic, E. Dzib, X. Zarate, F. Ortíz-Chi, Z. H. Cui, J. Barroso and G. Merino, *Chem. Sci.*, 2021, **12**, 6699–6704.
20 G. Castillo-Toraya, F. Ortíz-Chi, J. Barroso, M. Orozco-Ic, L. Leyva-Parra and G. Merino, *Angew. Chem., Int. Ed.*, 2025, **64**, e202500292.
21 L. M. Yang, E. Ganz, Z. Chen, Z. X. Wang and P. V. R. Schleyer, *Angew. Chem., Int. Ed.*, 2015, **54**, 9468–9501.
22 A. I. Boldyrev, X. Li and L. S. Wang, *Angew. Chem., Int. Ed.*, 2000, **39**, 3307–3310.
23 H. Fang, H. Jing, A. Zhang, H. Ge, Z. Yao, P. J. Brothers and X. Fu, *J. Am. Chem. Soc.*, 2016, **138**, 7705–7710.
24 F. Ebner and L. Greb, *J. Am. Chem. Soc.*, 2018, **140**, 17409–17412.
25 C. Shan, S. Dong, S. Yao, J. Zhu and M. Driess, *J. Am. Chem. Soc.*, 2023, **145**, 7084–7089.
26 J. C. Guo and S. D. Li, *J. Mol. Struct.:THEOCHEM*, 2007, **816**, 59–65.
27 A. N. Alexandrova, M. J. Nayhouse, M. T. Huynh, J. L. Kuo, A. V. Melkonian, G. Chavez, N. M. Hernando, M. D. Kowal and C. P. Liu, *Phys. Chem. Chem. Phys.*, 2012, **14**, 14815–14821.
28 J. Xu and Y. H. Ding, *J. Comput. Chem.*, 2015, **36**, 355–360.
29 J. C. Guo, C. Q. Miao and G. M. Ren, *Comput. Theor. Chem.*, 2014, **1032**, 7–11.
30 J. C. Guo, H. X. Wu, G. M. Ren, C. Q. Miao and Y. X. Li, *Comput. Theor. Chem.*, 2016, **1083**, 1–6.
31 J. J. Sui, J. Xu and Y. H. Ding, *Dalton Trans.*, 2016, **45**, 56–60.
32 L. Q. Zhao, J. C. Guo and H. J. Zhai, *Phys. Chem. Chem. Phys.*, 2022, **24**, 7068–7076.
33 Y. X. Jin and J. C. Guo, *Int. J. Mol. Sci.*, 2024, **25**, 2819.
34 X. H. Yin, H. L. Zeng, X. B. Liu, X. L. Xu, H. G. Xu, G. Merino, W. j Zheng and Z. H. Cui, *Angew. Chem., Int. Ed.*, 2025, **64**, e202415789.
35 M. H. Wang, X. Dong, Z. H. Cui, M. Orozco-Ic, Y. H. Ding, J. Barroso and G. Merino, *Chem. Commun.*, 2020, **56**, 13772–13775.
36 M. H. Wang, D. H. Fei, C. Chen, Y. Q. Liu, S. Pan and Z. H. Cui, *Chem. Phys. Chem.*, 2023, **24**, e202300257.
37 V. Vassilev-Galindo, S. Pan, K. J. Donald and G. Merino, *Nat. Rev. Chem.*, 2018, **2**, 0114.
38 J. O. C. Jimenez-Halla, Y. B. Wu, Z. X. Wang, R. Islas, T. Heine and G. Merino, *Chem. Commun.*, 2010, **46**, 8776–8778.
39 Y.-B. Wu, Y. Duan, H.-G. Lu and S.-D. Li, *J. Phys. Chem. A*, 2012, **116**, 3290–3294.
40 S. Pan, J. L. Cabellos, M. Orozco-Ic, P. K. Chattaraj, L. Zhao and G. Merino, *Phys. Chem. Chem. Phys.*, 2018, **20**, 12350–12355.
41 Z. H. Cui, V. Vassilev-Galindo, J. L. Cabellos, E. Osorio, M. Orozco, S. Pan, Y. H. Ding and G. Merino, *Chem. Commun.*, 2017, **53**, 138–141.
42 A. C. Castro, G. Martínez-Guajardo, T. Johnson, J. M. Ugalde, Y.-B. Wu, J. M. Mercero, T. Heine, K. J. Donald and G. Merino, *Phys. Chem. Chem. Phys.*, 2012, **14**, 14764–14768.
43 X. Y. Zhang and Y. H. Ding, *Comput. Theor. Chem.*, 2014, **1048**, 18–24.
44 Y. Pei, W. An, K. Ito, P. V. R. Schleyer and X. C. Zeng, *J. Am. Chem. Soc.*, 2008, **130**, 10394–10400.
45 J. C. Guo, Y. X. Cheng and X. F. Wu, *Comput. Theor. Chem.*, 2020, **1180**, 112824.
46 L. Leyva-Parra, L. Diego, D. Inostroza, O. Yañez, R. Pumachagua-Huertas, J. Barroso, A. Vásquez-Espinal, G. Merino and W. Tiznado, *Chem. – Eur. J.*, 2021, **27**, 16701–16706.
47 C. Adamo and V. Barone, *J. Chem. Phys.*, 1999, **110**, 6158–6170.
48 S. Grimme, S. Ehrlich and L. Goerigk, *J. Comput. Chem.*, 2011, **32**, 1456–1465.
49 F. Weigend and R. Ahlrichs, *Phys. Chem. Chem. Phys.*, 2005, **7**, 3297–3305.
50 F. Ortiz-Chi and G. Merino, Mérida, México 2020.
51 A. Ramirez-Manzanares, J. Peña, J. M. Azpiroz and G. Merino, *J. Comput. Chem.*, 2015, **36**, 1456–1466.
52 P. Fuentealba, L. Von Szentpaly, H. Preuss and H. Stoll, *J. Phys. B: At. Mol. Phys.*, 1985, **18**, 1287.
53 A. Bergner, M. Dolg, W. Küchle, H. Stoll and H. Preuß, *Mol. Phys.*, 1993, **80**, 1431–1441.
54 R. A. Kendall, T. H. Dunning Jr and R. J. Harrison, *J. Chem. Phys.*, 1992, **96**, 6796–6806.
55 D. E. Woon and T. H. Dunning Jr, *J. Chem. Phys.*, 1993, **98**, 1358–1371.
56 A. K. Wilson, D. E. Woon, K. A. Peterson and T. H. Dunning Jr, *J. Chem. Phys.*, 1999, **110**, 7667–7676.
57 K. Raghavachari, G. W. Trucks, J. A. Pople and M. Head-Gordon, *Chem. Phys. Lett.*, 1989, **157**, 479–483.
58 T. J. Lee and P. R. Taylor, *Int. J. Quantum Chem.*, 1989, **36**, 199–207.

59 J. M. Millam, V. r Bakken, W. Chen, W. L. Hase and H. B. Schlegel, *J. Chem. Phys.*, 1999, **111**, 3800–3805.
60 H. B. Schlegel, J. M. Millam, S. S. Iyengar, G. A. Voth, A. D. Daniels, G. E. Scuseria and M. J. Frisch, *J. Chem. Phys.*, 2001, **114**, 9758–9763.
61 M. J. Frisch, G. W. T., H. B. Schlegel, G. E. Scuseria, M. A. Robb, J. R. Cheeseman, G. Scalmani, V. Barone, B. Mennucci, G. A. Petersson, H. Nakatsuji, M. Caricato, X. Li, H. P. Hratchian, A. F. Izmaylov, J. Bloino, G. Zheng, J. L. Sonnenberg, M. Hada, M. Ehara, K. Toyota, R. Fukuda, H. Borkent, W. Laarhoven, J. Hasegawa, M. Ishida, T. Nakajima, Y. Honda, O. Kitao, H. Nakai, T. Vreven, J. J. Montgomery, J. E. Peralta, F. Ogliaro, M. Bearpark, J. J. Heyd, E. Brothers, K. N. Kudin, V. N. Staroverov, R. Kobayashi, J. Normand, K. Raghavachari, A. Rendell, J. C. Burant, S. S. Iyengar, J. Tomasi, M. Cossi, N. Rega, N. J. Millam, M. Klene, J. E. Knox, J. B. Cross, V. Bakken, C. Adamo, J. Jaramillo, R. Gomperts, R. E. Stratmann, O. Yazyev, A. J. Austin, R. Cammi, C. Pomelli, J. W. Ochterski, R. L. Martin, K. Morokuma, V. G. Zakrzewski, G. A. Voth, P. Salvador, J. J. Dannenberg, S. Dapprich, D. Daniels, O. Farkas, J. B. Foresman, J. V. Ortiz, J. Cioslowski and D. J. Fox, *Gaussian 16, Revision B.01*, Gaussian Inc., Wallingford, CT, 2016.
62 K. B. Wiberg, *Tetrahedron*, 1968, **24**, 1083–1096.
63 A. E. Reed, R. B. Weinstock and F. Weinhold, *J. Chem. Phys.*, 1985, **83**, 735–746.
64 E. D. Glendening, C. R. Landis and F. Weinhold, *J. Comput. Chem.*, 2019, **40**, 2234–2241.
65 D. Y. Zubarev and A. I. Boldyrev, *Phys. Chem. Chem. Phys.*, 2008, **10**, 5207–5217.
66 T. Lu and F. Chen, *J. Comput. Chem.*, 2012, **33**, 580–592.
67 W. Humphrey, A. Dalke and K. Schulten, *J. Mol. Graphics*, 1996, **14**, 33–38.
68 H. S. Fernandes, S. F. Sousa and N. M. Cerqueira, *J. Chem. Inf. Model.*, 2019, **59**, 4519–4523.
69 M. Blanco, A. Martín Pendás and E. Francisco, *J. Chem. Theory Comput.*, 2005, **1**, 1096–1109.
70 T. Keith and T. K. Gristmill, *Software*, Overland Park, KS, USA, 2019.
71 G. T. Te Velde, F. M. Bickelhaupt, E. J. Baerends, C. Fonseca Guerra, S. J. van Gisbergen, J. G. Snijders and T. Ziegler, *J. Comput. Chem.*, 2001, **22**, 931–967.
72 E. van Lenthe, A. Ehlers and E. J. Baerends, *J. Chem. Phys.*, 1999, **110**, 8943–8953.
73 E. Van Lenthe and E. J. Baerends, *J. Comput. Chem.*, 2003, **24**, 1142–1156.
74 A. Michalak, R. L. DeKock and T. Ziegler, *J. Phys. Chem. A*, 2008, **112**, 7256–7263.
75 M. P. Mitoraj, A. Michalak and T. Ziegler, *J. Chem. Theory Comput.*, 2009, **5**, 962–975.
76 M. P. Mitoraj, A. Michalak and T. Ziegler, *Organometallics*, 2009, **28**, 3727–3733.
77 C. Møller and M. S. Plesset, *Phys. Rev.*, 1934, **46**, 618.
78 P. Pyykkö, *J. Phys. Chem.*, 2015, **119**, 2326–2337.
79 S. Alvarez, *Dalton Trans.*, 2013, **42**, 8617–8636.
80 P. Muller, *Pure Appl. Chem.*, 1994, **66**, 1077–1184.